CRS4

Centre for Advanced Studies,

Research and Development in Sardinia

Uta - (CA)

Numerical determination of hydrodynamic coefficients for manoeuvring without free surface effects

Date: November 30^{th} 1999

by:

M. Mulas and M. Talice

Fluid Dynamics and Combustion Area

abstract

Manoeuvring conditions for the S60 ship model are presented in this work. Numerical simulations have been carried out for steady-drift motion, steady-turning and a combination of steady-turning with drift angle. Two configurations of the S60 have been considered: with bolck coefficient C_b equal to 0.6 and 0.8. The goal of the work was to investigate the capabilities of a in-house developed CFD code to accurately reproduce lateral forces (normal to the direction of motion) and z-moments (with respect to the axis normal to the free surface) for such flow conditions. No effects of the free surface have been considered, thus approaching towing tank situations with negligible Froude number.

The inviscid Euler approximation has been used instead of the full turbulent RANS approximation. It is believed that, similarly to external aerodynamics problems, inviscid simulation can accurately represent lateral forces and moments about the z-axis. Furthermore it allows a substantial reduction of both the grid-generation process and the CPU time needed.

The calculations have been carried out with an innovative approach to numerical towing tank simulations: the fully compressible Euler and Navier-Stokes equations are marched in time with a Jameson-like method, namely an outer multi-grid acceleration algorithm, and an inner multi-stage Runge-Kutta explicit scheme. Beside a preconditioning matrix, to allow for incompressible flow simulations, the present method makes use of an arbitrary equation of state and high order TVD schemes based on Roe's approximate Riemann solver. The arbitrary equation of state used in this work is given in terms of water compressibility coefficients β and χ (respectively at constant pressure and at constant temperature).

Results presented compare well to the few experimental data available, and show that the numerical code represents a reliable and computationally efficient tool for investigating the typical manoeuvring situations of interest.

Contents

1 Physical model

Typical towing tank numerical simulations for monoeuvring are carried out with Reynolds Averaged Navier-Stokes (RANS) models. RANS simulations require a well resolved boundary layer throughout the whole hull surface. Boundary layer resolution, in terms of non-dimensional distances y^+ of the first grid line close to the solid surface, depends however upon the turbulence model employed. The algebraic Baldwin-Lomax model requires $y^+ < 3$, which means that there must be at least two grid lines within the laminar sub-layer. Low-Reynolds 2-equation models are even more demanding: they typically need $y^+ < 1$ in order to integrate down to the solid surface the equations for both the turbulent kinetic energy κ and the turbulent dissipation ϵ, or any other variant such as ω or τ. Wall-function 2-equation models are more robust and less accurate: the first line must be somewhere in log-region of the boundary layer, with y^+ between, say, 50 and 200, then the universal "law of the wall" is used to extrapolate values to the solid boundaries.

As the Reynolds numeber is increased, the y^+ requirement makes the grid generation process more and more severe: in order to keep the same y^+, the physical grid spacing has to become smaller and smaller. At Reynolds number of the order 10^6 to 10^7, typical meshes for RANS simulations are of the order of 500,000 nodes minimum. Simulations at the real Reynolds number (order of 10^8 to 10^9) would then need much larger meshes.

If inviscid computations were possible, a great saving in grid generation and computational resourses would be possible. Inviscid Euler simulations require meshes with aspect ratios of order unity in the vicinity of the solid surfaces. A good Euler mesh for such hydrodinamic cases is made of about 150,000 nodes only and, more important, it does not need to scale with the Reynolds number.

Use of the inviscid physical model poses however the question whether an inviscid computation can develop the correct vorticity (and the correct circulation and lift as a consequence) when the incoming flow is irrotational. This is a very intriguing issue which is however not very much debated in the literature, with the remarkable exception of Hirsch [1]. As a matter of fact, large scale vorticity generation, transport and evolution is a truly inviscid and inertial mechanism independent of the fluid viscosity. It does however need a trigger to get started since the incoming flow is free of vorticity. Real flows have the viscous boundary layer as the actual trigger, whereas in inviscid simulations this triggering function is played by the always present numerical diffusion (truncation errors), which is higher in high gradients regions (namely close to the sharp edges of the solid surfaces, such as bow and stern). No matter which the triggering mechanism is, once started the full rotational Euler equations system should be able to converge to the real large-scale rotational solution.

More than 30 years of inviscid numerical aerodynamics show that this is the case and that lateral forces (lift) and z-moments (pitching moments) are accurately represented by Euler codes provided that no boundary layer separation occurs. In such cases the Euler equations system represents the limit for infinite Reynolds number of the full RANS system, and provide the correct pressure and velocity fields, and the vorticity field as a consequence. As the Reynolds number grows higher and higher, the attached turbulent boundary layer becomes thinner and thinner. The actual surface geometry and the "inviscid" geometry (displaced by a length equal to the boundary layer displacement thickness) become closer and closer to each other. Typical curves of non-dimensional force and moment coefficients plotted against the Reynolds number become flat in the high Reynolds number region (typically above about 10^5) for external flows over slender bodies. The flat region represents the region where the inviscid simulation ("infinite" Reynolds number) can be used. The only non-dimensional independent parameter in high Reynolds number regimes is represented by the Froude number which measures the effect of the free surface upon the non-dimensional forces and moments. In this work such an effect has not been considered.

In 3D towing tank simulations the situation is even easier, with respect to the 3D wings of external aerodynamics, due to the fact that streamwise boundary layer separation does not occur even at high angles of attack and at high loads. The typical suction side boundary layer separation, due to high angles of attack, is in fact unavoidable in 2D wing profiles (infinite span) as well as in high aspect ratio 3D wings (high span to chord ratios); it is however almost impossible for the very small aspect ratio ship hulls, as will be shown in the results section. The main requirement which allows to make use of the inviscid simulation instead of the full RANS simulation is thus at hand: namely *high Reynolds numbers and no boundary layer separations*.

Though in presence of very few experimental data available for comparison, the results of the present work show with clear evidence that inviscid simulation is indeed able to produce reliable lateral forces and z-moments for the S60 hulls.

2 Numerical model

The code **Karalis** solves the fully compressible Euler and Navier-Stokes equations where all couplings between dynamics and thermodynamics are allowed. This is the most general mathematical model for all fluid flows. Continuity, momentum and total energy equations are fully coupled by a general equation of state of the form

$$\phi = \phi(p, T)$$

where ϕ represents any thermodynamic variable, such as density, enthalpy or speed of sound for instance.

At Mach number close to zero the acoustic perturbation speed is much bigger than the propagation velocity of the perturbations moving with fluid particles. In mathematical words, as the fluid speed becomes lower and lower the eigenvalues of the system of equations become very much spread giving rise to an ill conditioned Euler matrix at very low speeds: the ratio of acoustic speed to particle speed grows unbounded. In order to apply the fully compressible formulation also to incompressible flows (or to flows of incompressible fluids), a preconditioning techniques must then be used. Multiplication of the matrix of the system of the Euler equations by a preconditioning matrix artificially changes the characteristic speeds (matrix eigenvalues) at which signals propagate in fluids: the use of the preconditioning technique alters the acoustic perturbation speed, making it of the same order of magnitude of the fluid velocity. In other words, the real incompressible world is transferred into a highly compressible one, in which the compressible formulation of the numerical algorithm does recover its original efficiency.

The preconditioned system of the Euler equations, in compact vector form, is given by:

$$\frac{\partial Q}{\partial t} + \mathbf{P} \left(\frac{\partial E}{\partial x} + \frac{\partial F}{\partial y} + \frac{\partial G}{\partial z} \right) + \mathbf{P} \left(viscous \quad fluxes \right) = 0$$

Merkle's preconditioning technique [2] was chosen because it can easily formulated for abitrary equations of state. Merkle's preconditioning matrix $\mathbf{P}$ is given by:

$$\mathbf{P} = \mathbf{M}\mathbf{M}_m^{-1}$$

where $\mathbf{M}$ represents the Jacobian matrix of the vector of conservative variables Q with respect to the vector of the so-called viscous-primitive variables Q_v:

$$\mathbf{M} = \left(\frac{\partial Q}{\partial Q_v} \right) \qquad Q = \begin{pmatrix} \rho \\ \rho \vec{V} \\ \rho E \end{pmatrix} \qquad Q_v = \begin{pmatrix} p \\ \vec{V} \\ T \end{pmatrix}$$

and where $\mathbf{M}_m$ represents a modified version of $\mathbf{M}$. Note that no modification (i.e. $\mathbf{M} = \mathbf{M}_m$ and $\mathbf{P} = \mathbf{I}$) brings back to the original not preconditioned system.

The matrix $\mathbf{M}$ contains arbitrary thermodynamics in terms of derivatives of density and enthalpy with respect to pressure and temperature ($\rho_p\ \rho_T\ h_p\ h_T$), while the matrix $\mathbf{M}_m$ contains "modified" thermodynamics in terms of ρ_p^m and ρ_T^m. Rescaling of the characteristic speeds is obtained with proper choice for "modified" values of the fluid compressibility coefficients. At steady-state (i.e. $\partial Q/\partial t = 0$) the preconditioned system shares the same solution of the original non preconditioned system.

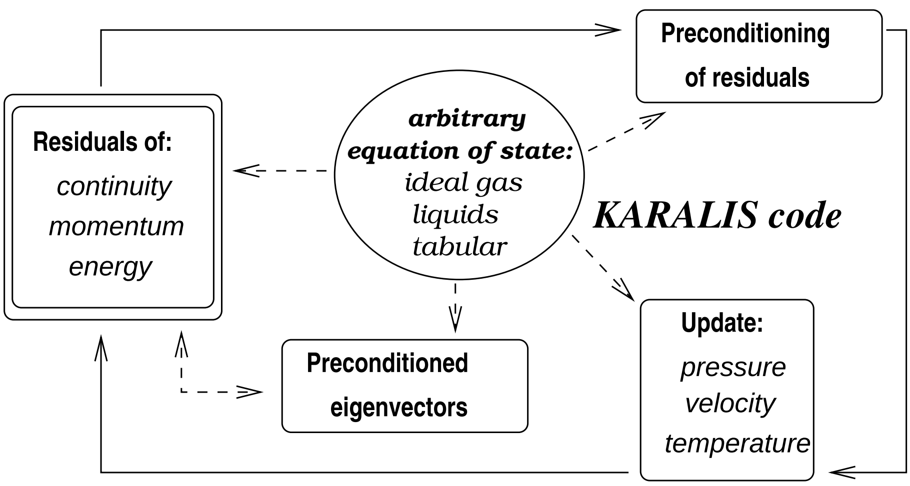

The system of equations to be solved is kept in conservative form, for it represents the basic principles of conservation of mass, momentum and total energy (kinetic and internal energy). In order to modify an originally compressible code for ideal gases, continuity, momentum and total energy residuals must however be updated not in terms of the conservative variables Q, but in terms of the so-called viscous-primitive variables Q_v, namely pressure, temperature and the velocity components. This is done multiplying the preconditioned system by $\mathbf{M}^{-1}$ to the left:

$$\frac{\partial Q_v}{\partial t} + \mathbf{M}_m^{-1} \left(\frac{\partial E}{\partial x} + \frac{\partial F}{\partial y} + \frac{\partial G}{\partial z} \right) + \mathbf{M}_m^{-1} \ (viscous \ \ fluxes) = 0$$

Once $\vec{V}$, p and T are updated, arbitrary thermodynamics can be supplied and the iterative numerical procedure can continue. A V-cycle Coarse Grid Correction Multi-Grid algorithm is used, together with a 5-stage Runge-Kutta explicit time-marching method, to accelerate convergence to a steady state. This formulation, typical of aerodynamic flows, shows an excellent efficiency even for incompressible flows, once equipped with Merkle's preconditioner. In the case of liquid fluid, the equation of state is given in terms of the compressibility coefficients at constant pressure and constant temperature, typically denoted by β and χ. The picture above shows a skematic representation of **Karalis** code.

Various second order TVD schemes are used to compute convective fluxes through the Finite-Volume cell interfaces. Differently from popular scalar artificial dissipation schemes, TVD schemes are based on the decomposition of the Euler equations into waves (decomposition into characteristic variables) so that proper upwinding can be applied to each wave depending on the sign of the corresponding wave speed. This implies an eigenvector decomposition of the (now preconditioned) Euler matrix:

$$\mathbf{D}_p = \mathbf{PD} \equiv \mathbf{P}\ (\mathbf{A}n_x + \mathbf{B}\ n_y + \mathbf{C}n_z)$$

where:

$$\mathbf{A} = \left(\frac{\partial E}{\partial Q}\right) \quad \mathbf{B} = \left(\frac{\partial F}{\partial Q}\right) \quad \mathbf{C} = \left(\frac{\partial G}{\partial Q}\right)$$

so that the numerical evaluation of the flux vector H:

$$H = E\ n_x + F\ n_y + G\ n_z$$

is given by:

$$H^*_{i+1/2} = \frac{H_i + H_{i+1}}{2} - \frac{1}{2}\ \mathbf{P}^{-1}\ \mathbf{R}_p\ |\Lambda_p|\ \mathbf{L}_p(Q_{i+1} - Q_i)$$

where $\mathbf{R}_p$ and $\mathbf{L}_p$ represent the matrices of right and left eigenvectors of $\mathbf{D}_p$, and Λ_p represents the diagonal matrix whose elements are $\mathbf{D}_p$ eigenvalues. All matrices contain arbitrary thermodynamics through $\mathbf{P}$.

In the Finite-Volume framework at each cycle (iteration) the solution algorithm is given by:

$$\frac{\partial Q_v}{\partial t} = \mathbf{M}_m^{-1}\ \frac{1}{\Delta V}\ (RES^m_{inv} + RES_{vis})$$

and it is made of the following 4 steps represented skematically in the previuous picture:

- calculation of the conservative residuals of continuity, momentum and energy;

  viscous residuals are unchanged;

  inviscid residuals are modified if TVD schemes are used;

- preconditioning of all residuals
- updating in terms of p, $\vec{V}$, and T
- arbitrary thermodynamics is supplied at each step

Karalis has been extensively validated for typical test cases of incompressible fluid dynamics such as the *lid driven cavity* and the *backward facing step* for instance, showing convergence rates typical of compressible fluid dynamics.

3 Test cases

Two different configurations of the S60 Series hull will be examined here, namely with the block coefficient Cb = 0.6 and Cb = 0.8, which will be indicated from now on Cb06 and Cb08, respectively.

3.1 Grids

Two different multi-blocks and multi-levels grids have been used for the present simulations. The grid used for the Cb06 case is an O-H type mesh with 113 nodes on the hull in the stream-wise direction, and 41 nodes in the crosswise direction, with some 150,000 nodes total in 6 blocks. The grid used for the Cb08 case is an O-O type mesh with 65 and 25 nodes on the hull surface in the stream-wise and crosswise direction, respectivelly. The overall grid points number being also about 150,000.

Figures 3 and 4 show the enlargements of three grid sections around the hull. Sections called **a**, **b**, and **c** in the following, are made at 10% of the hull length from the bow, at middle and at 10% from the stern.

3.2 Examined Cases List

Three manoeuvring conditions sets have been simulated: **Steady Drift**, **Steady Turning** and the **Composition of Steady Drift** and **Steady Turning**. Table 1 summarizes all the simulations which have been performed (R/L represents the ratio between the curvature radius to the hull length, and β represents the drift angle).

Case	Symbol	β	R/L
Steady Drift	sd-02	2	∞
	sd-05	5	∞
	sd-10	10	∞
Steady Turning	st-r2	0	2
	st-r3	0	3
	st-r4	0	4
Steady Turning	st+sd-r2	10	2
+	st+sd-r3	10	3
Steady Drift	st+sd-r4	10	4

Table 1: Examined Cases Summary

Figure 1 shows the typical convergence histories of all cases simulated. Convergence plots show the maximum x-momentum residual versus the multi-grid cycle.

The maximum residual at the iteration (multi-grid cycle in this case) *no.n* is defined as:

$$R_{max} = log_{10} \frac{RES^n_{max}}{RES^0_{max}}$$

where, RES^0_{max} represents the maximum residual at iteration *no*.0, that is, at the beginning of the simulation. When $RES_{max} = -8$, for instance, then the maximum residual has decreased by eight orders of magnitude with respect to the beginning of the simulation. The Cb06 cases always showed better convergences with respect to the corresponding Cb08 cases. Simulations have been run on a PC-Linux 450 MHz Pentium III processor, and take some 1 hour CPU-time for 100 multigrid cycles. Engineering convergence of force and moment coefficients are generally reached when $R_{max} = -3.5,\ 4$.

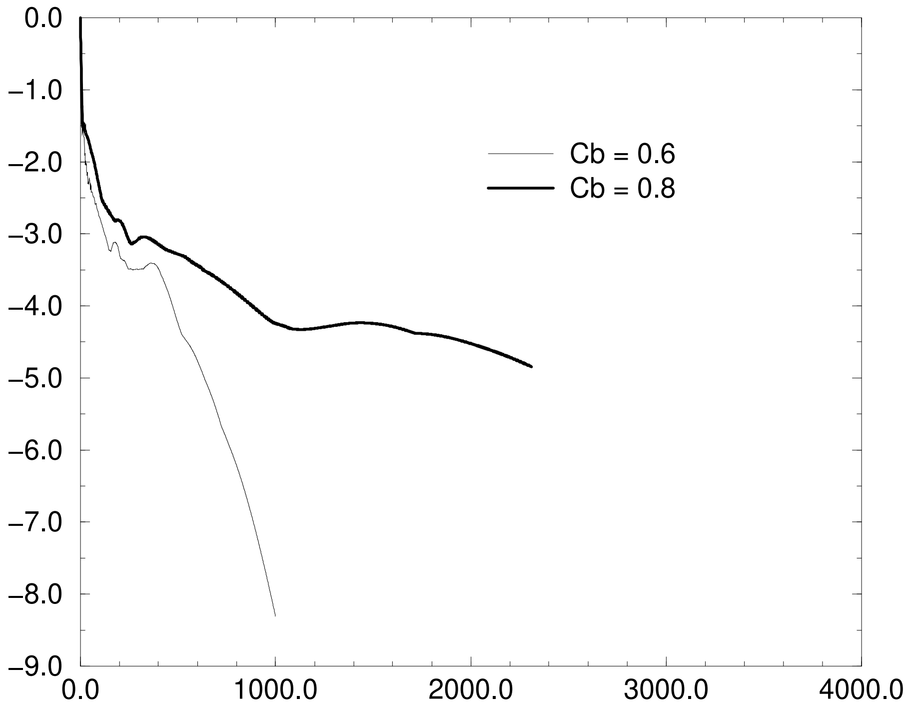

Figure 1: typical convergence histories of x-momentum residuals versus multi-grid cycles

Figure 2 shows the convergence histories for the steady turning cases with the smallest radius of curvature combined with the drift angle. These two cases are the only ones which failed to converge to a steady-state solution. Convergence plots most likely suggest the presence of a physical unsteadiness in these very much

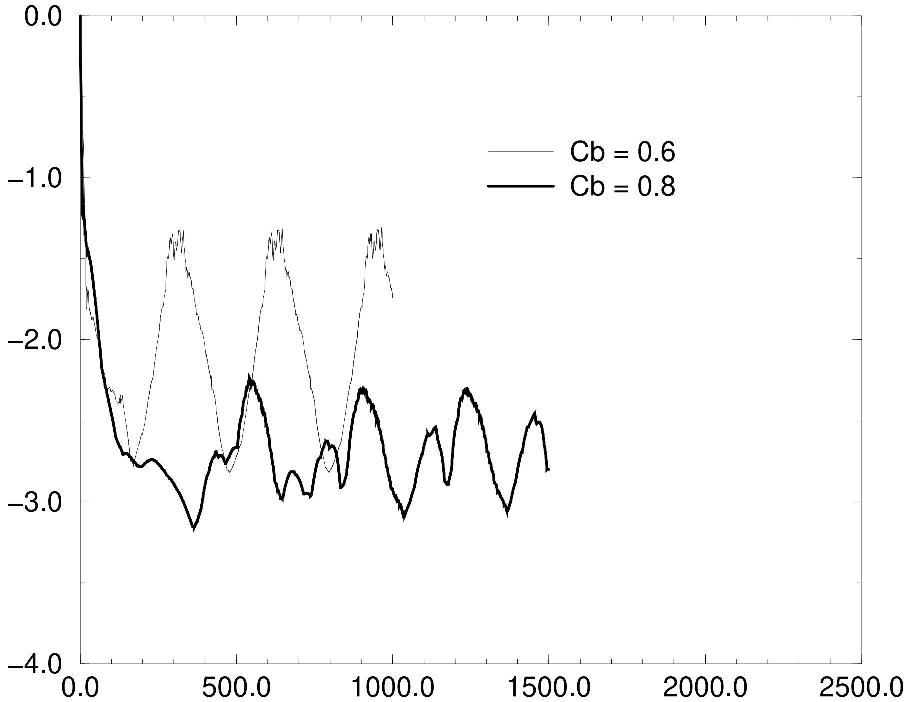

Figure 2: convergence histories of x-momentum residuals versus multi-grid cycles for $R/L = 2$ and $\beta = 10^o$.

loaded flow conditions, probably a periodic vortex shedding associated with a Stroual number. They will be discussed in more details in the results section.

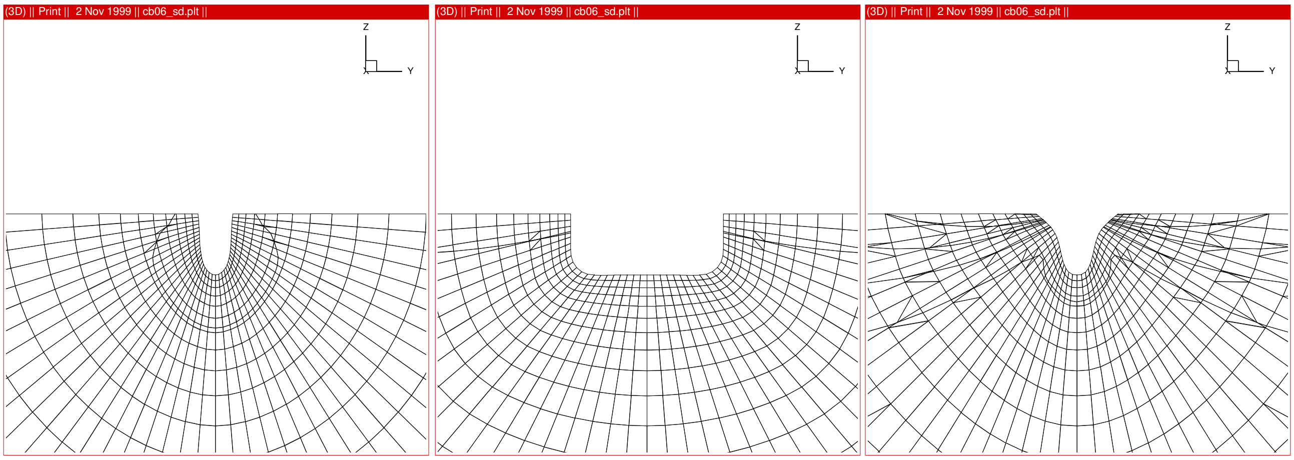

Figure 3: Cb=0.6: grid at sections a, b and c

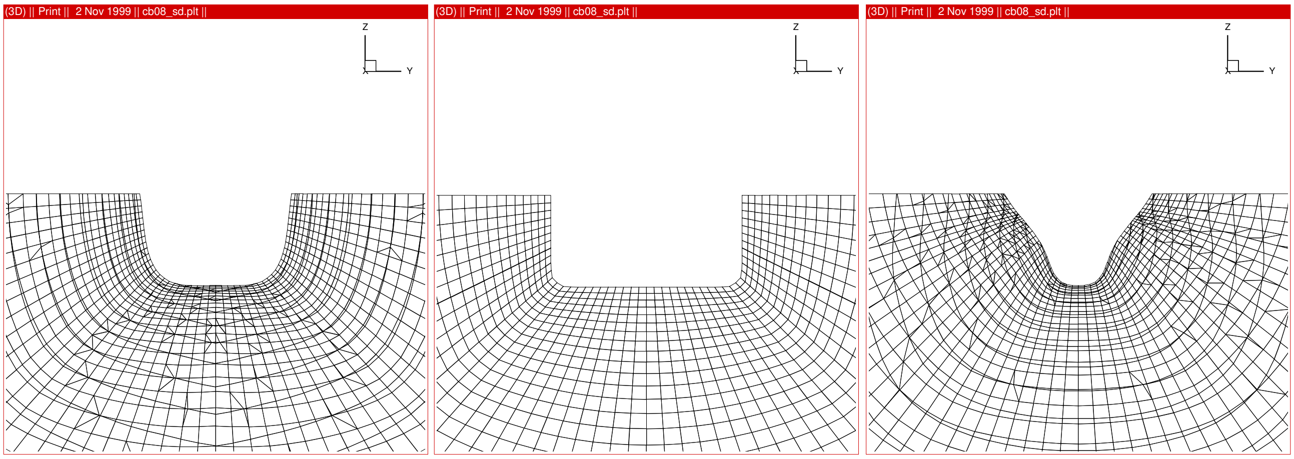

Figure 4: Cb=0.8: grid at sections a, b and c

4 Results

4.1 hydrodinamic coefficients

In the authors' knowledge the only available work which allows to make a comparison between numerical and experimental data in the chosen conditions of zero Froude number and high Reynolds number, is the one by J. F. Longo [3]. This work provides data for the Steady Drift case only, for the Cb06 hull. Table 2 shows the measured values for the C_f and C_M coefficients (the non-dimensional lateral force and z-moment respectively).

Fr	β	C_f	C_M
0.10	2	0.003	-0.00021
0.10	5	0.008	-0.00052
0.10	10	0.021	-0.00103

Table 2: Cb06 Steady Drift: Experimental Data Summary

The experiments show that below Froud number Fr = 0.16, the free surface effects become negligible, so that a comparison between the computed case (Fr = 0) and the experiments (Fr = 0.10) makes sense.

Tables 3 and 4 summarize all the computed results. The exam of the values reported for C_f and C_M in Tab. 3 shows an excellent agreement of the computed C_f with experimental data. Computed C_M are excellent as well, though a bit underestimated (within 10% error).

Case	β	R/L	F_y	C_f	M_z	C_M
sd-02	2	∞	0.277	0.0032	-0.099	-0.00019
sd-05	5	∞	0.762	0.0089	-0.246	-0.00047
sd-10	10	∞	1.773	0.0207	-0.500	-0.00095
st-r2	0	2	-0.552	-0.0064	-0.882	-0.00168
st-r3	0	3	-0.421	-0.0049	-0.540	-0.00103
st-r4	0	4	-0.316	-0.0037	-0.420	-0.0080
st+sd-r2	10	2	2.06	0.024	-1.555	-0.00296
st+sd-r3	10	3	1.884	0.022	-1.190	-0.00227
st+sd-r4	10	4	1.799	0.021	-1.163	-0.00222

Table 3: Cb06 Result Summary

Figures 5 to 10 show the computed C_f and C_M for both hulls considered. Though with no experimental data available for the steady-turning case (with and without combination with drift angle) calculated C_f and C_M look reasonable: the case with higher block coefficient C_b shows higher nondimensional moments and lower nondimensional forces with respect to the Cb06, when in presence of a drift angle. For the pure turning and no drift, the two hulls show very similar hydrodinamic coefficients: forces are much lower and negative because they represent the pressure gradient needed to balance the centrifugal forces.

Case	β	R/L	F_y	C_f	M_z	C_M
sd-02	2	∞	0.206	0.0017	-0.263	-0.00053
sd-05	5	∞	0.808	0.0066	-0.537	-0.00107
sd-10	10	∞	2.066	0.0168	-0.972	-0.00194
st-r2	0	2	-0.837	-0.0068	-0.916	-0.00183
st-r3	0	3	-0.581	-0.0047	-0.567	-0.00113
st-r4	0	4	-0.403	-0.0033	-0.395	-0.0079
st+sd-r2	10	2	2.30	0.0188	-1.850	-0.00370
st+sd-r3	10	3	1.993	0.0162	-1.652	-0.00330
st+sd-r4	10	4	2.082	0.0170	-1.494	-0.00300

Table 4: Cb08 Result Summary

4.2 velocity vector plots

4.2.1 steady drift

Reference [3] provides many details of the flow structure in terms of velocity vector plots for Fr = 0.16 and Fr = 0.316 in many cross sections. Though not explicitely stated, it is argued that they refer to the highest drift angle $\beta = 10^o$. Exam of the experimantal vector plots indicates that no streamwise boundary layer separation occurs. Due to the very small span to chord ratio typical of ship hulls, weakening of suction side boundary layer is prevented by new flow coming from the pressure side and passing below the ship hull. The overall motion from pressure to suction side generates a stationary vortex around the x-axis (direction of motion) along the whole length of the hull. The vortex, triggered by the viscous boundary layer, sustains itself by typical large scale inviscid and inertial kinetic energy transfer from the main flow motion. Mild crosswise boundary layer separation is noticeable from the plots: stronger at the front, and almost negligible around mid hull.

Figures from 11 to 16 show the computed velocity vector plots in the steady drift motion at the previously defined three cross sections for both the Cb06 and the Cb08 hull. The viewer is looking at the flow field from the hull's stern toward the bow. In any section the flow streams coming from the left hand side, pass below the hull and keep going from left to right. The x-vortex is missing in the computations, however the overall flow structure is very much close to that measured by the experiments. As a matter of fact, the accuracy of the computed hydrodinamic coefficients indicates that the experimentally detected local vortex structure does not influence the overall pressure and velocity field.

4.2.2 steady turning

Figures from 17 to 23 refer to the steady turning case with no drift. The overall flow structure is much different from the previous drift motion. Fluid particles are forced to follow a curvilinear trajectory, namely a circle which has radius equal to R/L. Again the viewer is looking at the flow field from the hull's stern toward the bow. In sections **a** the flow goes from left to right, like in the steady drift case. In sections **c** the flow goes from right to left. The angle of attack of the undisturbed flow on the hull surface is then not constant anymore: moving from the bow to the stern, the angle is positive at first, becomes negligible in the middle part of the hull and then assumes negative values in the stern region, as clearly visible from vector plots in the three sections. As a result, the flow moves below the hull from port to starboard side at the bow region, and viceversa at the stern region. This is the mechanism responsible for the generation of the vortexes shown in the figures. In the middle section of the hull the flow path has to invert the direction of its crossflow motion, and this generates the swirl. Figure 19 contributes to understand the overall flow structure showing the z-velocity component in three horizontal planes at constant **z** in the case of $R/L = 2$ for the Cb06 hull (above) and for the CB08 one (below). The exam of the figure allows to see how the flow is moving with negative z-velocity component around the lower side of the bow (blue colored zone), to assume positive component at the same side near the stern (red colored zone). The leftmost frame refers to a $z = const$ plane below the hull.

4.2.3 steady turning with drift

The combination of steady turning with the steady drift motion at angle of attack $\beta = 10^o$, is discussed here. As for the pure turning case, the same three radii of curvature ($R/L = 2$, 3 and 4) have been considered. Due to the imposed drift angle the undistrurbed curvilinear trajectories have positive incidence throughout the whole hull length, with decreasing intensity from bow to stern (with the exception of the smallest radius $R/L = 2$, for which the stern region still sees a small negative incidence). The value chosen for the drift angle was probably too high, and not very much realistic, though this condition allows to put in evidence the main character of this type of motion. The exam of the figures from 24 to 30 shows that even if the main features of the steady turning motion are still conserved here, the over imposition of the steady drift component, makes the vortexes in the middle section become smaller and moving from their original position below the hull surface, towards the right upper side. This behavior is confirmed in all the computed cases, but in the CB08 with R/L = 2, for which the vortex is not present at all (fig. 25). Figure 28 contributes to understand the overall flow structure showing the z-velocity component in three horizontal planes at constant **z** in the case of $R/L = 3$ for the Cb06 hull (above) and for the CB08 one (below). The case $R/L = 2$ was particularly loaded. For this case only, calculations show no steady-state convergence and indicate the possibility of a periodic regime, most likely with vortex oscillations that might be associated to a Stroual number.

5 Conclusions

The possibility of using an inviscid Euler mathematical model in order to determine lateral hydrodynamic forces and moments acting on the hull of a ship in maneuvering motion, has been investigated. The comparison, whenever possible, of the computed values with the experimental data, has shown an excellent agreement. The inviscid rotational model, due to its much less severe requirements in terms of computational grid and memory and CPU-time resources, can be extensively used in order to more efficiently investigate the maneuvering motion of different ship models. Last, but not least, the original "compressible" numerical model, equipped with a preconditioner, showed very good numerical efficiency.

A number of interesting issues remains to be investigated in the next future. Validation of the inviscid model with other ship hull geometries with available experimental data and time accurate simulations are among these issues, particularly in situations where physical unsteadiness and periodic motion are likely to develop. Full RANS simulations are also needed to validate the inviscid model and to compute resistance forces.

6 References

[1] C. Hirsch *"Numerical computation of internal and external flows. Volume 2."*, pagg. 395-401, Wiley 1990.

[2] C.L. Merkle *et al.* *"Computation of flows with arbitrary equations of state."*, AIAA J. vol.36, no.4, April 1998.

[3] J.F. Longo *"Effects of yaw model-scale ship flows."*, PhD thesis, University of Iowa, May 1996.

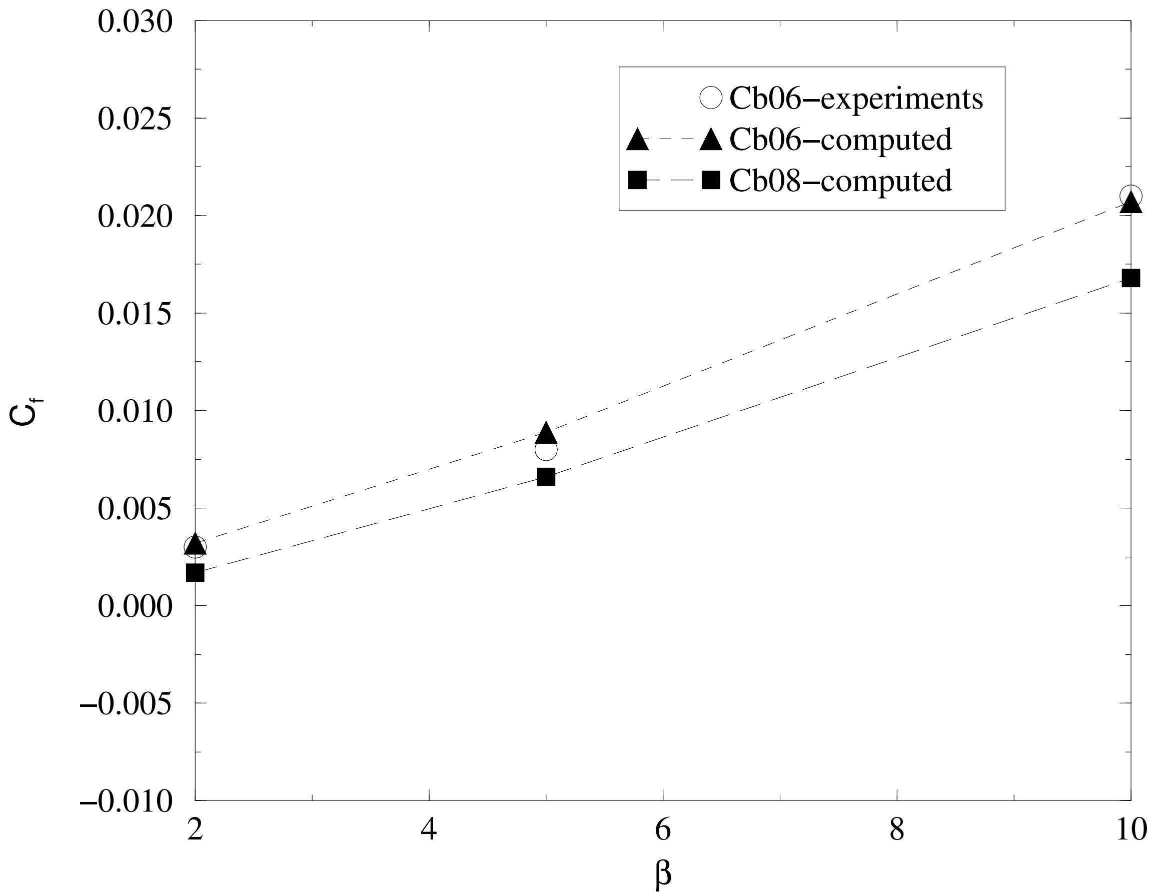

Figure 5: Steady Drift: C_f

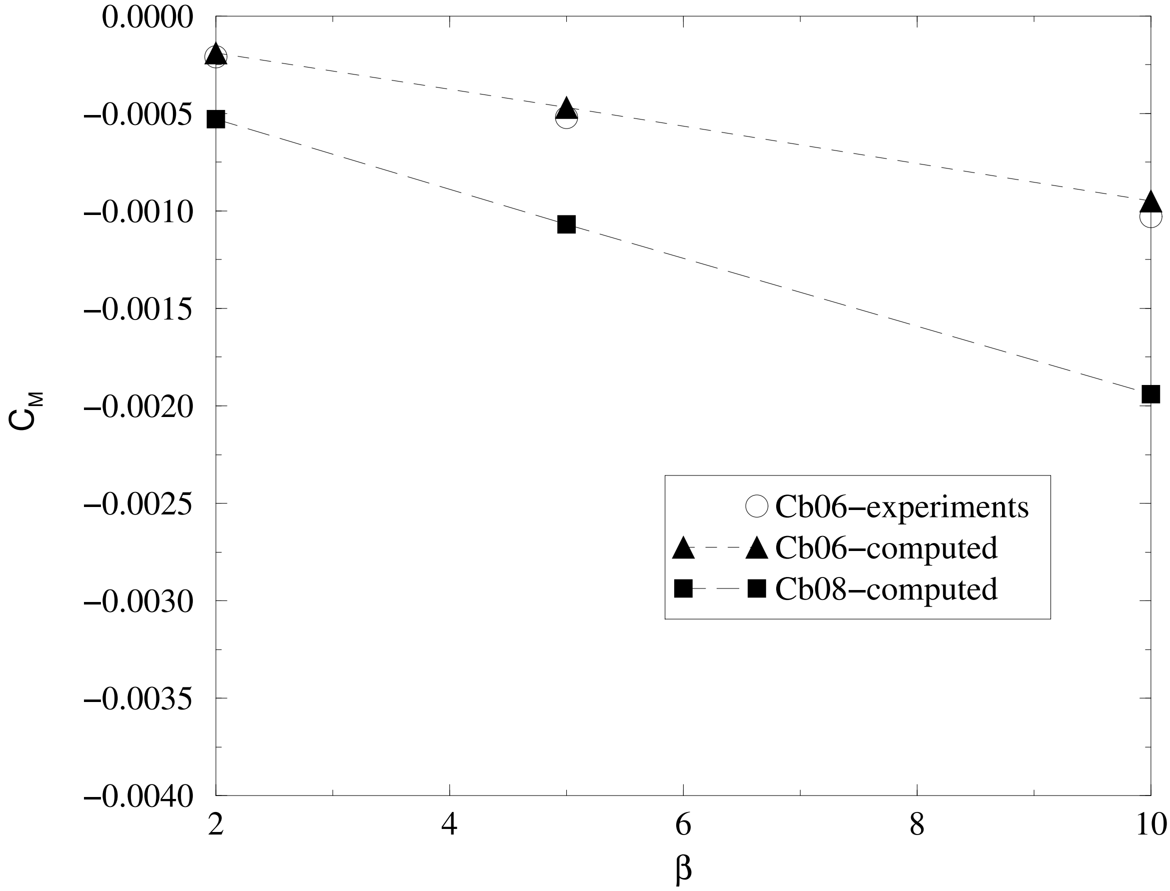

Figure 6: Steady Drift: C_m

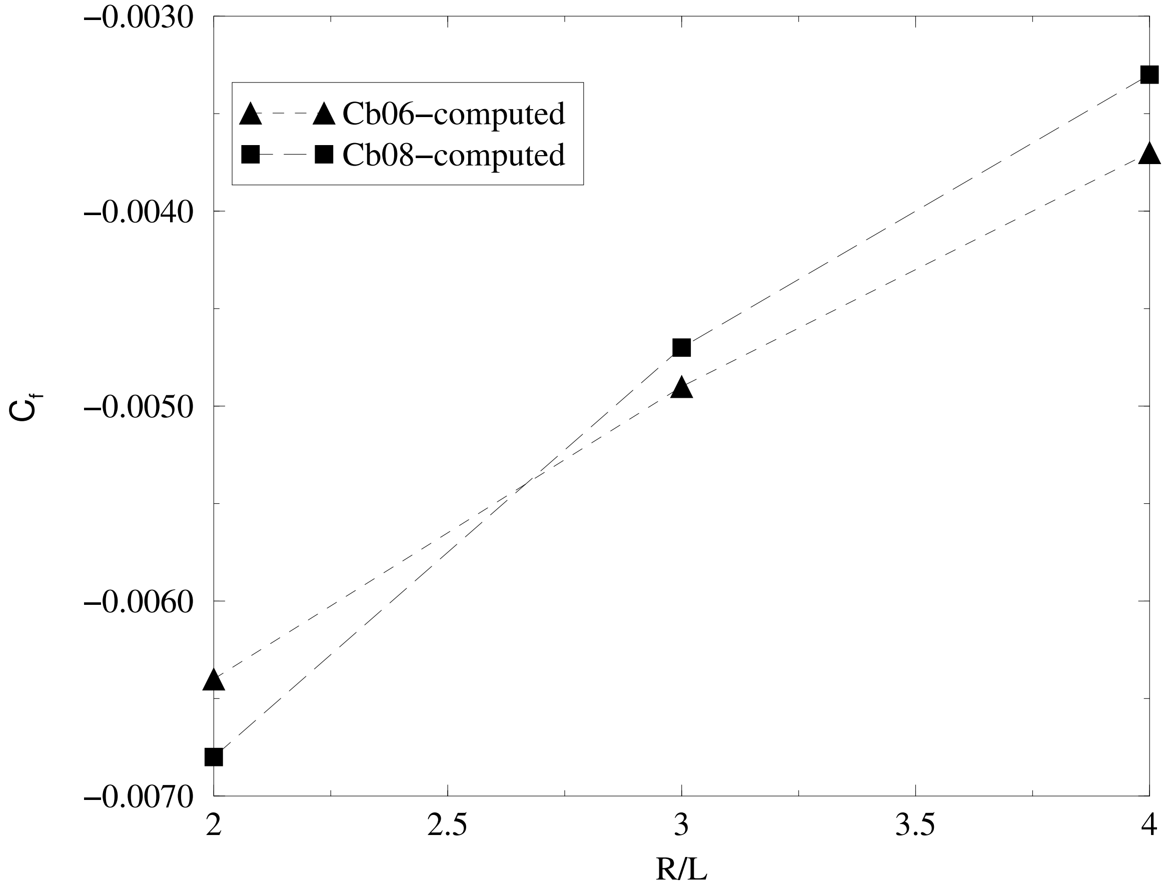

Figure 7: Steady Turning: C_f

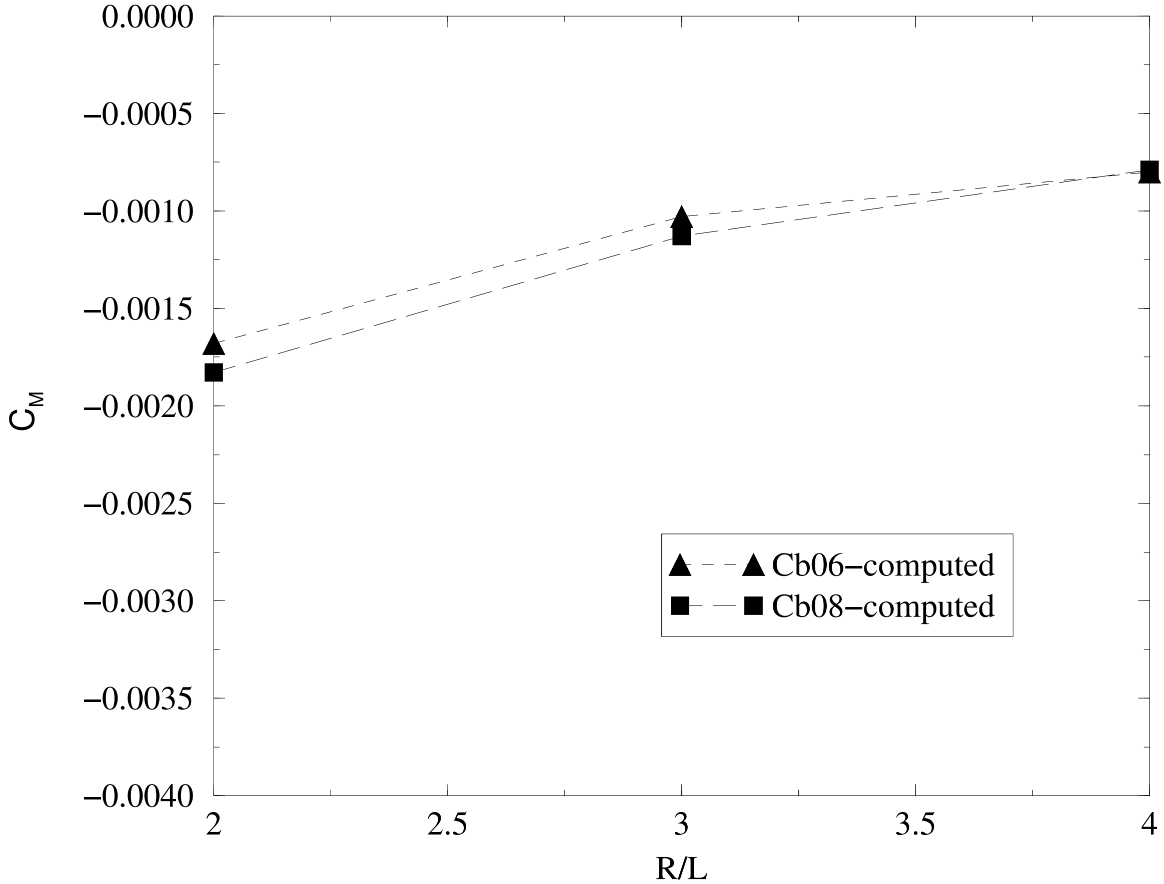

Figure 8: Steady Turning: C_m

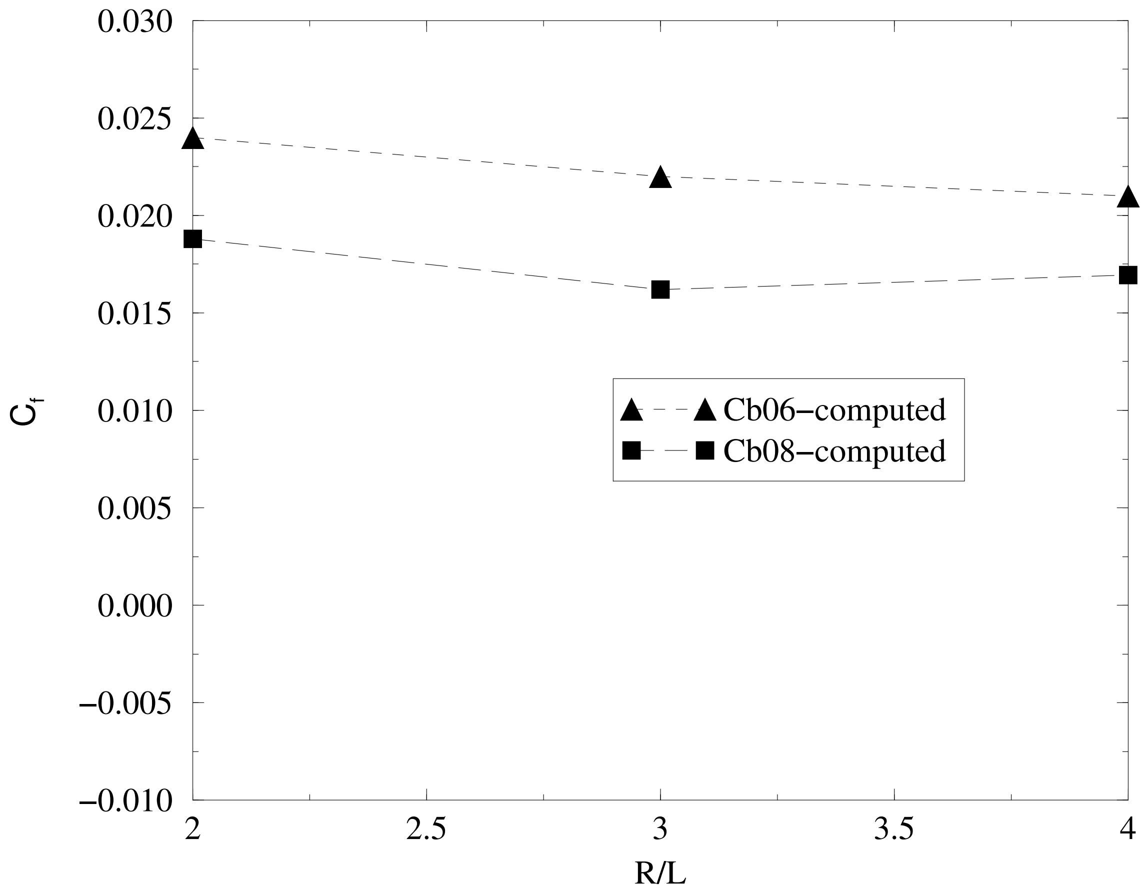

Figure 9: Steady Turning with $\beta = 10$: C_f

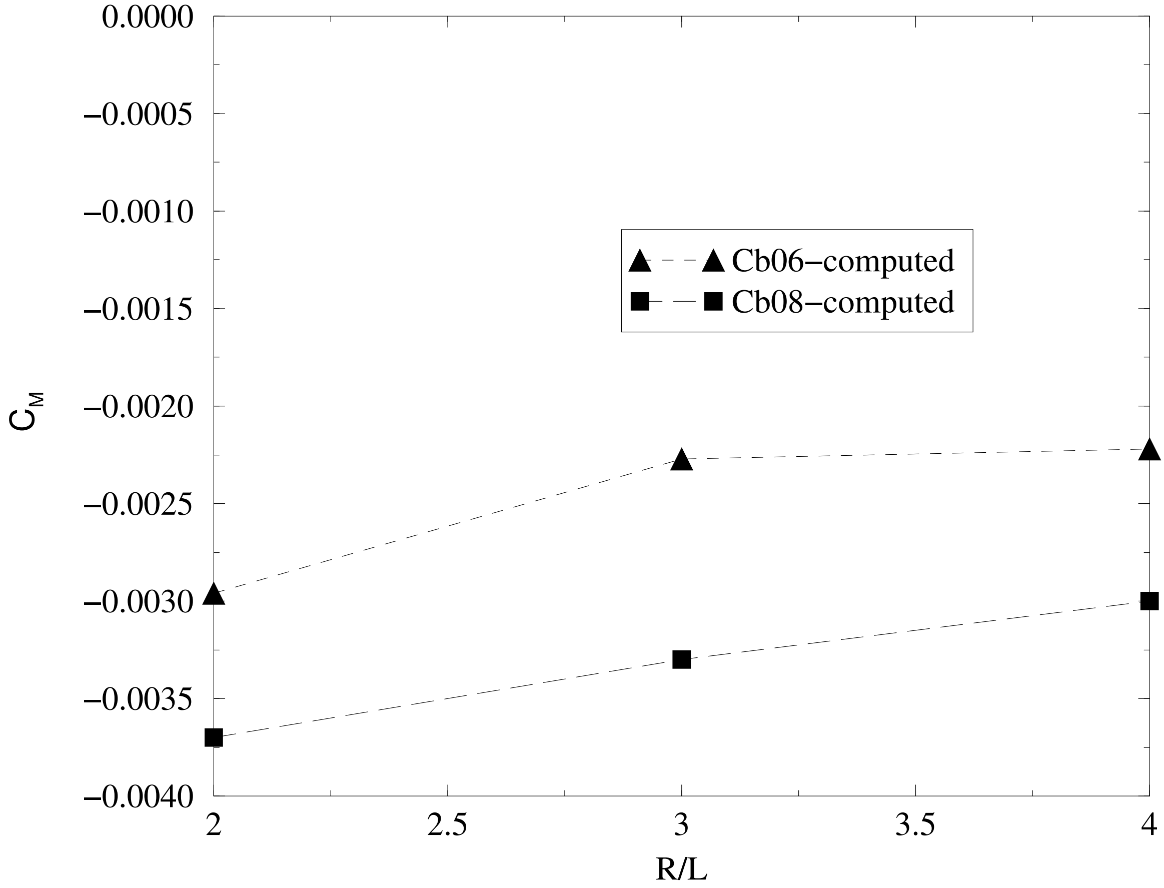

Figure 10: Steady Turning with $\beta = 10$: C_m

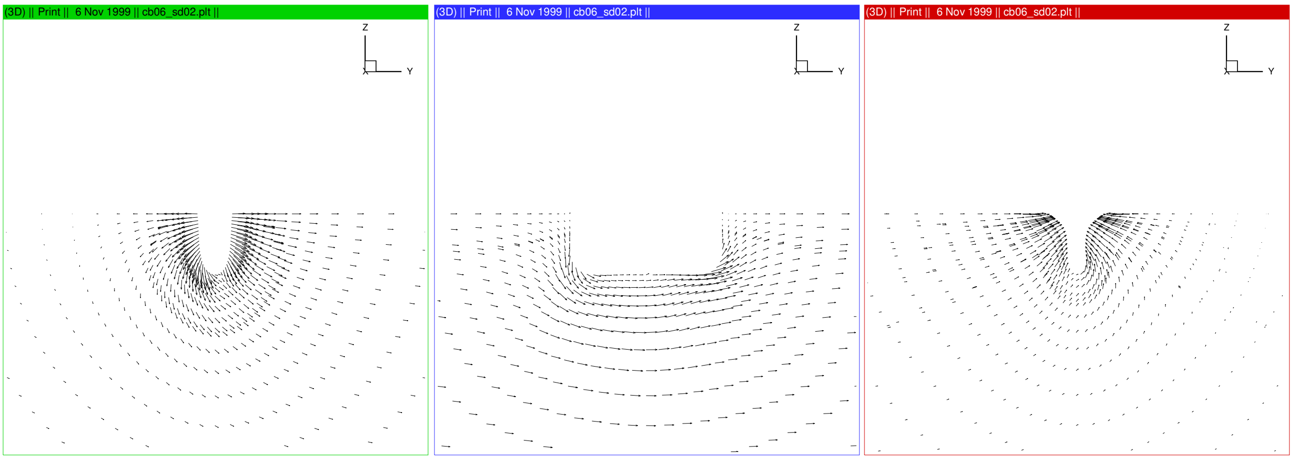

Figure 11: Cb=0.6, Steady Drift: β = 2; velocity vectors at sections a, b and c

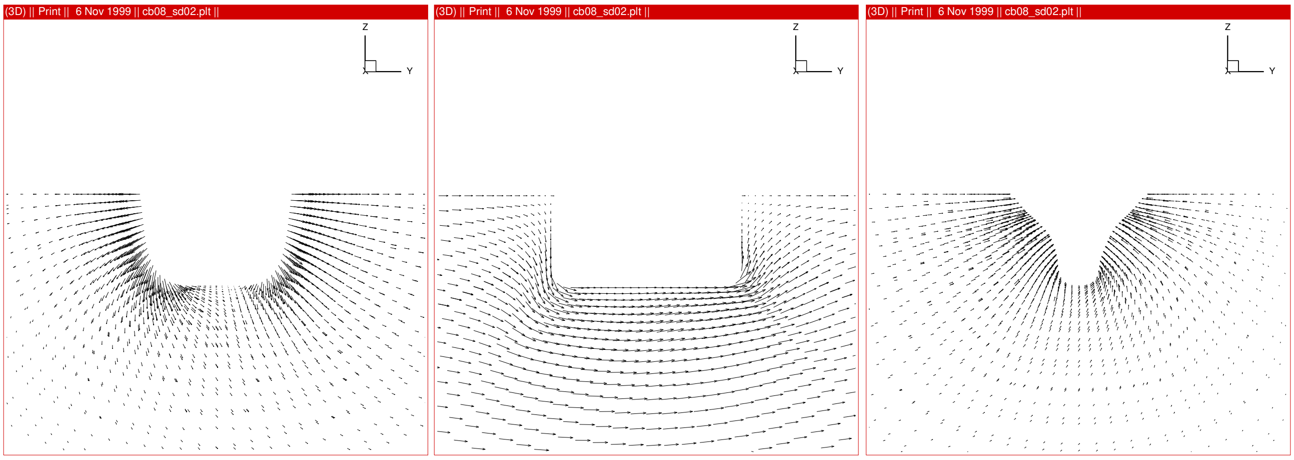

Figure 12: Cb=0.8, Steady Drift: β = 2; velocity vectors at sections a, b and c

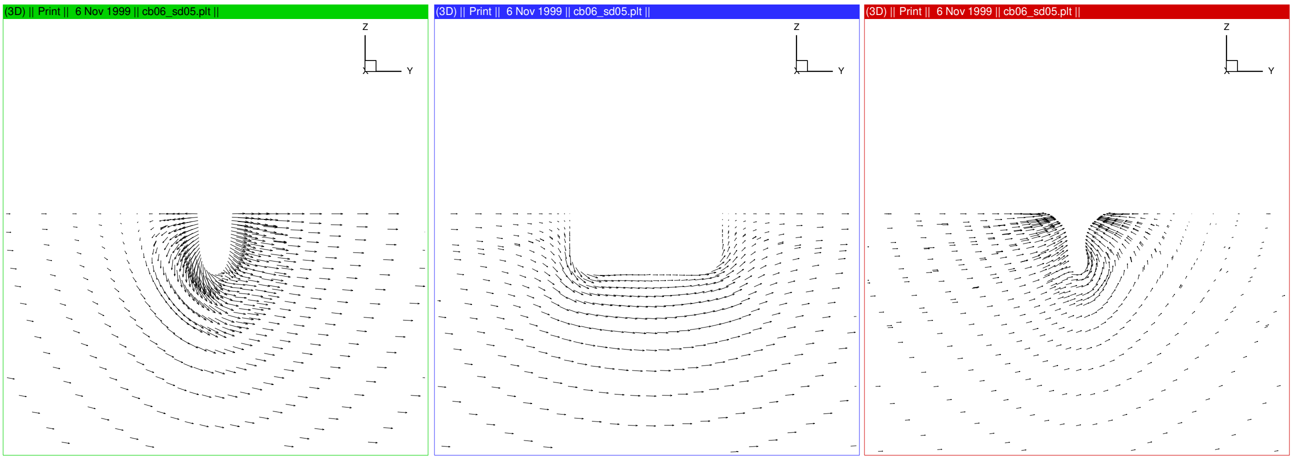

Figure 13: Cb=0.6, Steady Drift: $\beta = 5$; velocity vectors at sections a, b and c

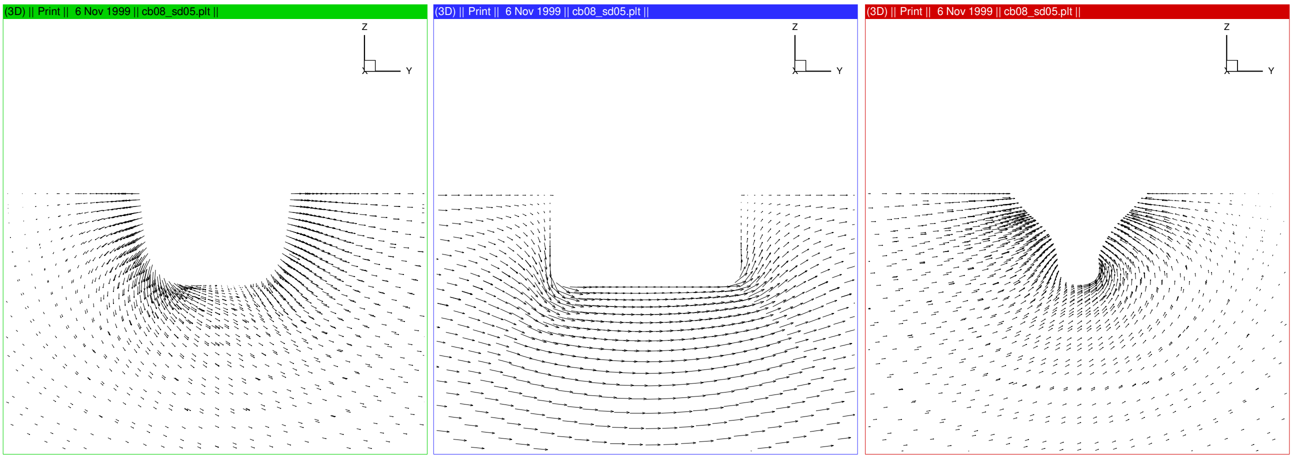

Figure 14: Cb=0.8, Steady Drift: $\beta = 5$; velocity vectors at sections a, b and c

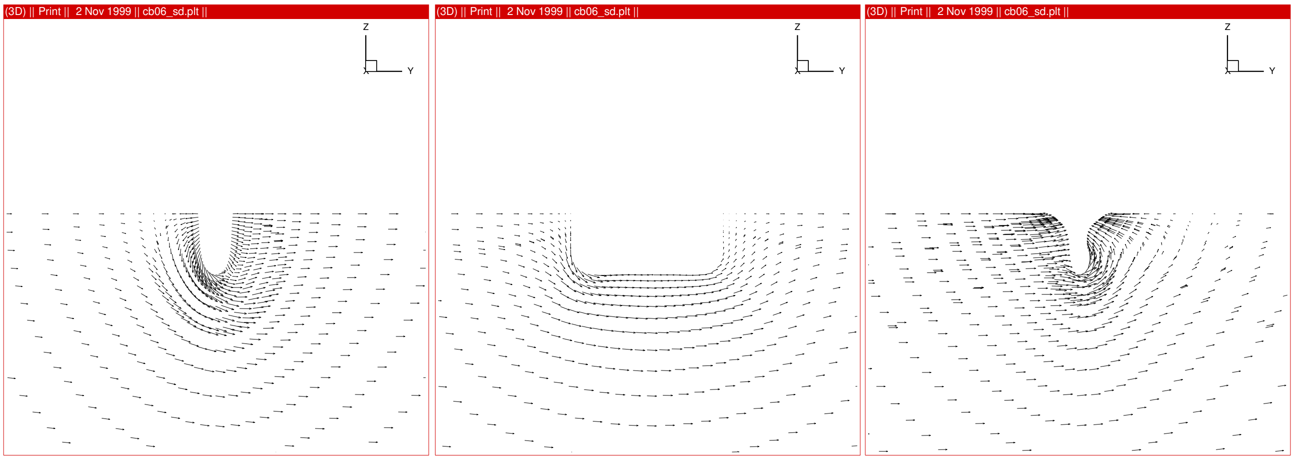

Figure 15: Cb=0.6, Steady Drift: β = 10; velocity vectors at sections a, b and c

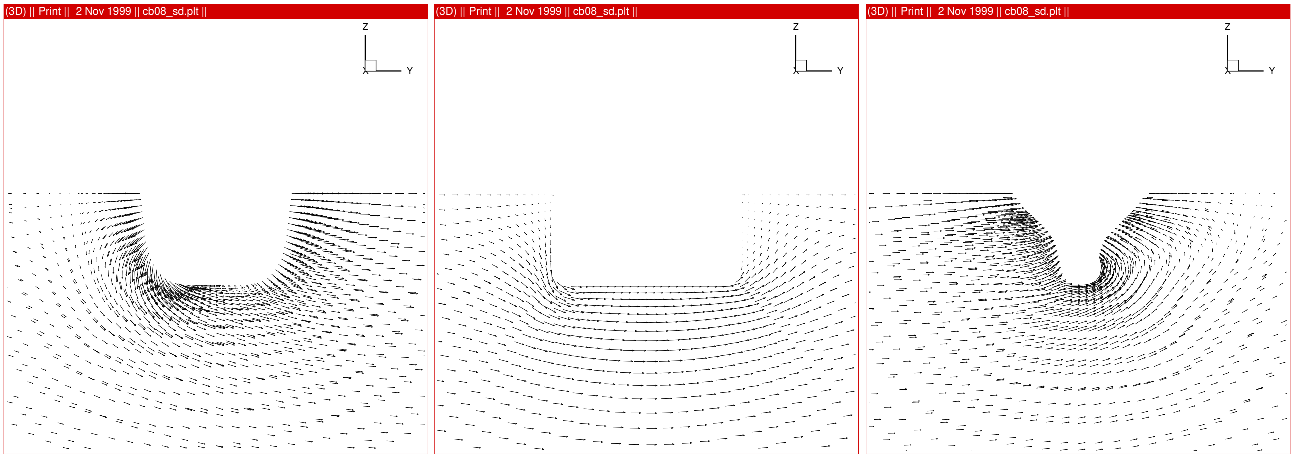

Figure 16: Cb=0.8, Steady Drift: β = 10;; velocity vectors at sections a, b and c

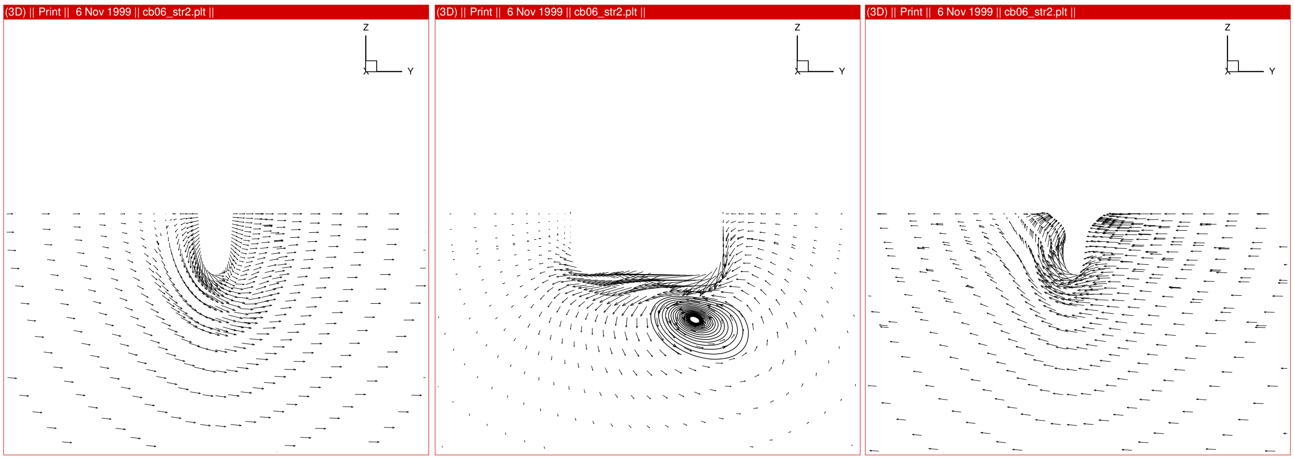

Figure 17: Cb=0.6, Steady Turning: R/L=2; velocity vectors at sections a, b and c

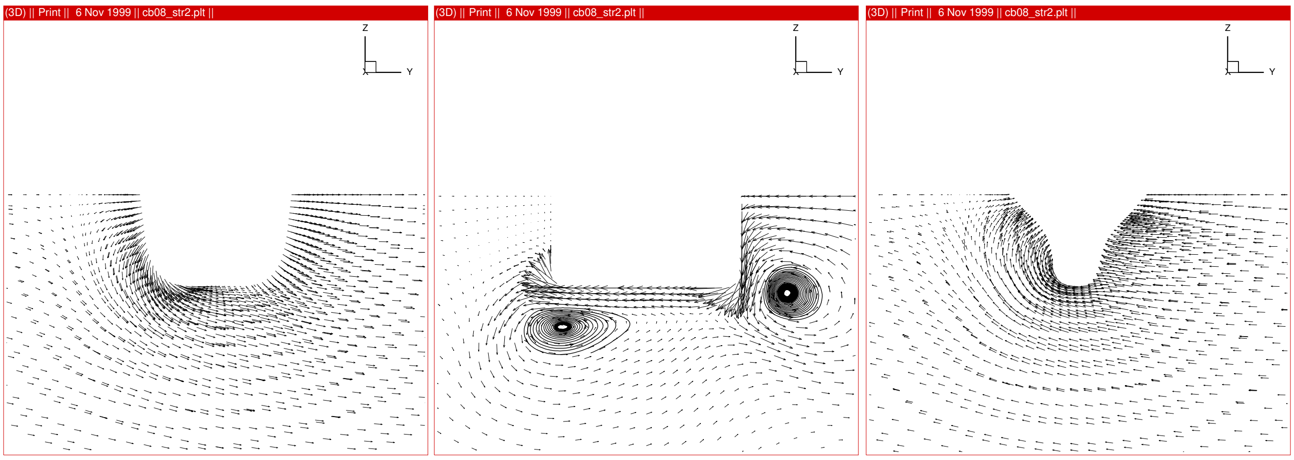

Figure 18: Cb=0.8, Steady Turning: R/L=2; velocity vectors at sections a, b and c

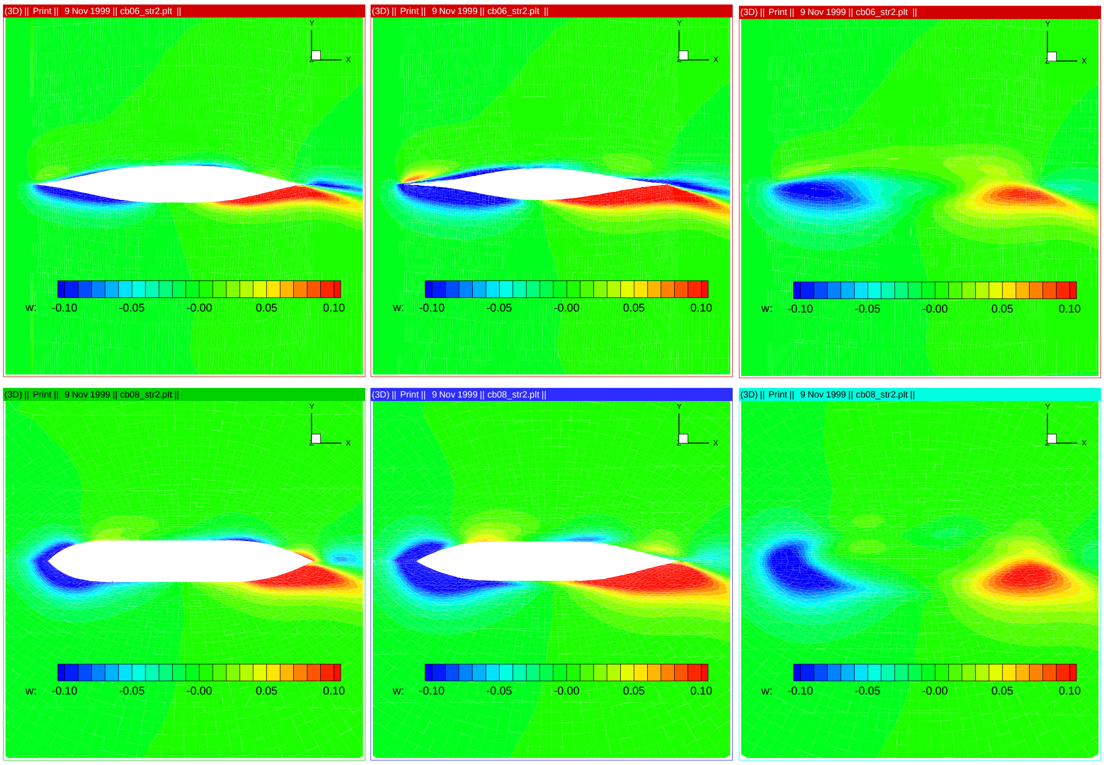

Figure 19: Cb=0.6 (top) and CB=0.8 (bottom): z-velocity contours plot; Steady Turning case R/L=2

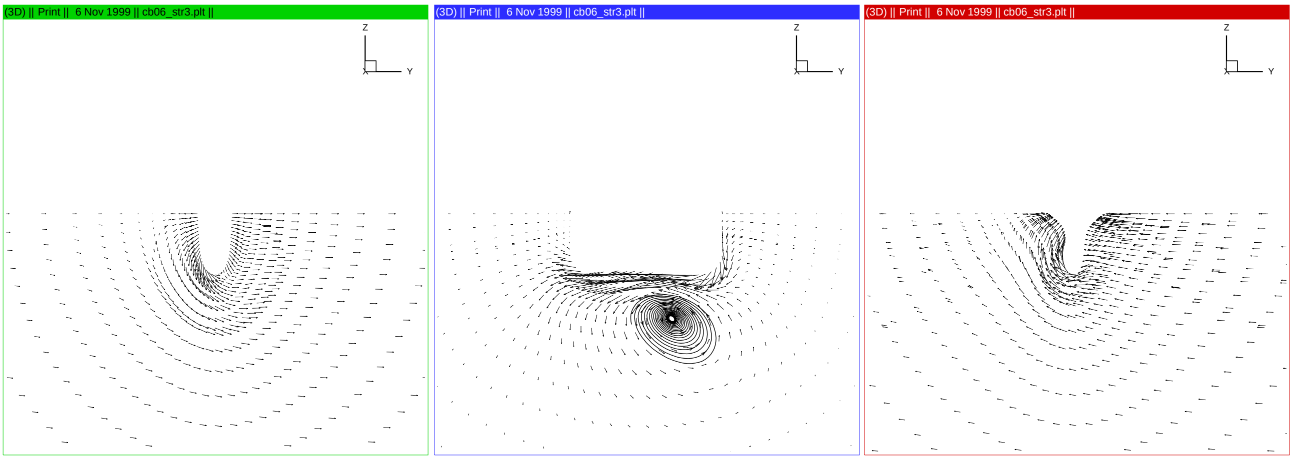

Figure 20: Cb=0.6, Steady Turning: R/L=3; velocity vectors at sections a, b and c

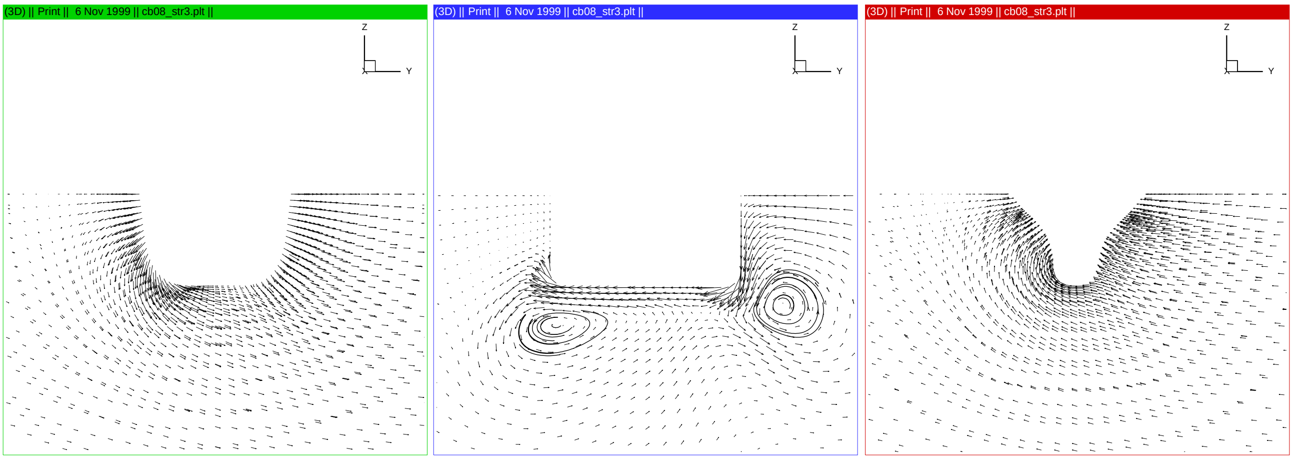

Figure 21: Cb=0.8, Steady Turning: R/L=3; velocity vectors at sections a, b and c

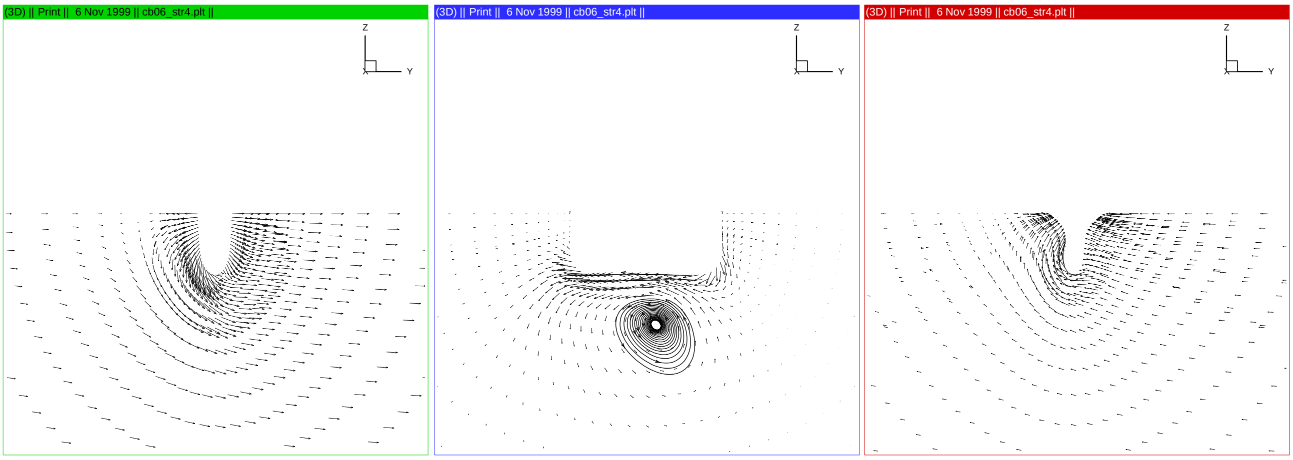

Figure 22: Cb=0.6, Steady Turning: R/L=4; velocity vectors at sections a, b and c

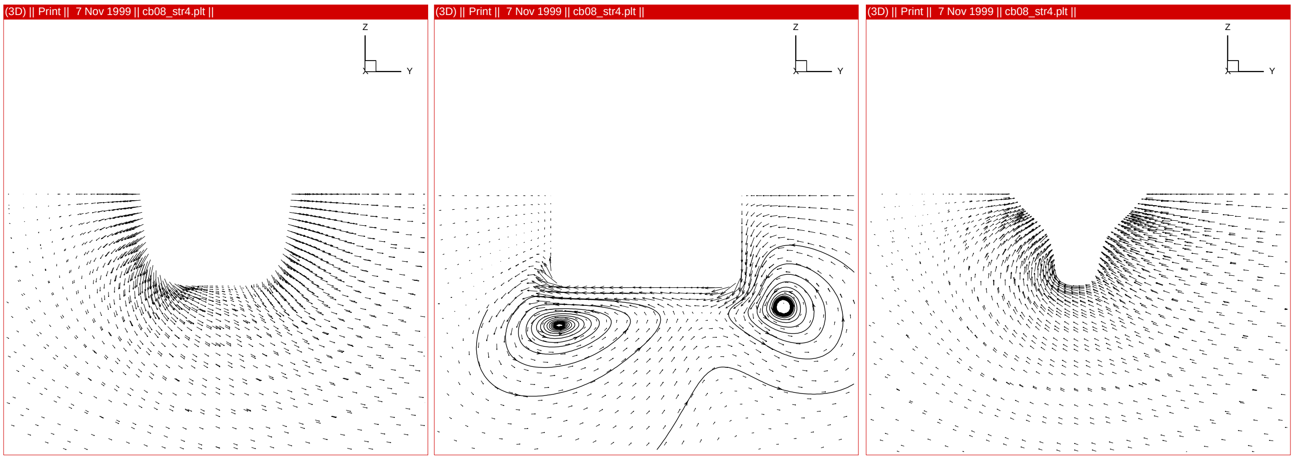

Figure 23: Cb=0.8, Steady Turning: R/L=4; velocity vectors at sections a, b and c

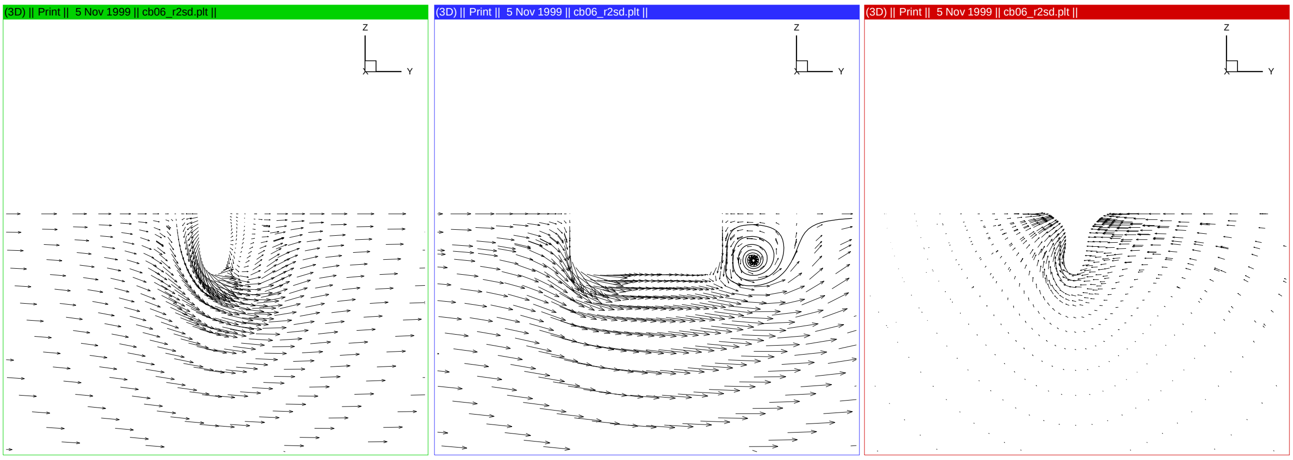

Figure 24: Cb=0.6, Steady Drift plus Turning: R/L=2, β=10

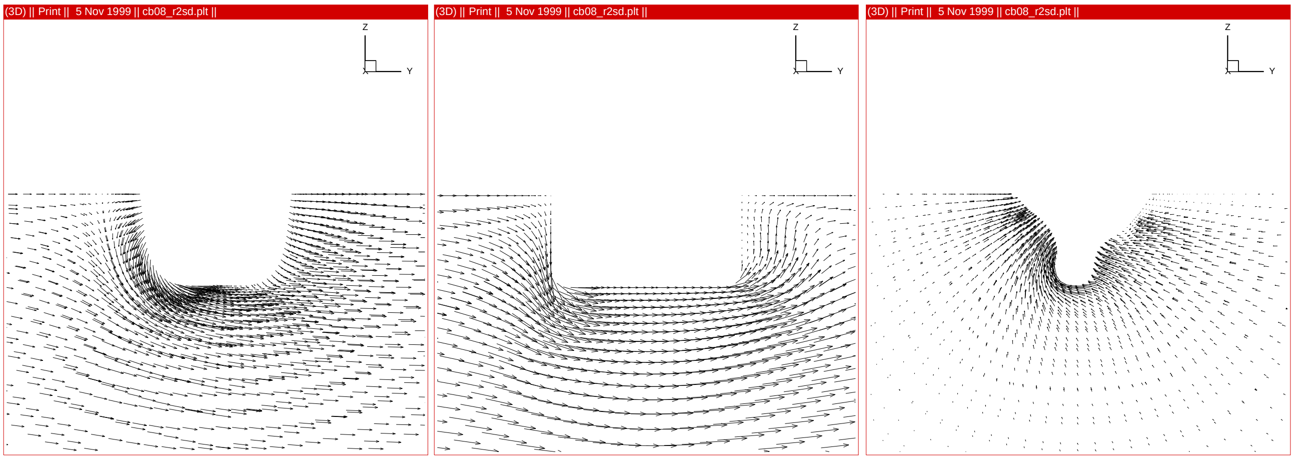

Figure 25: Cb=0.8, Steady Drift plus Turning: R/L=2, β=10

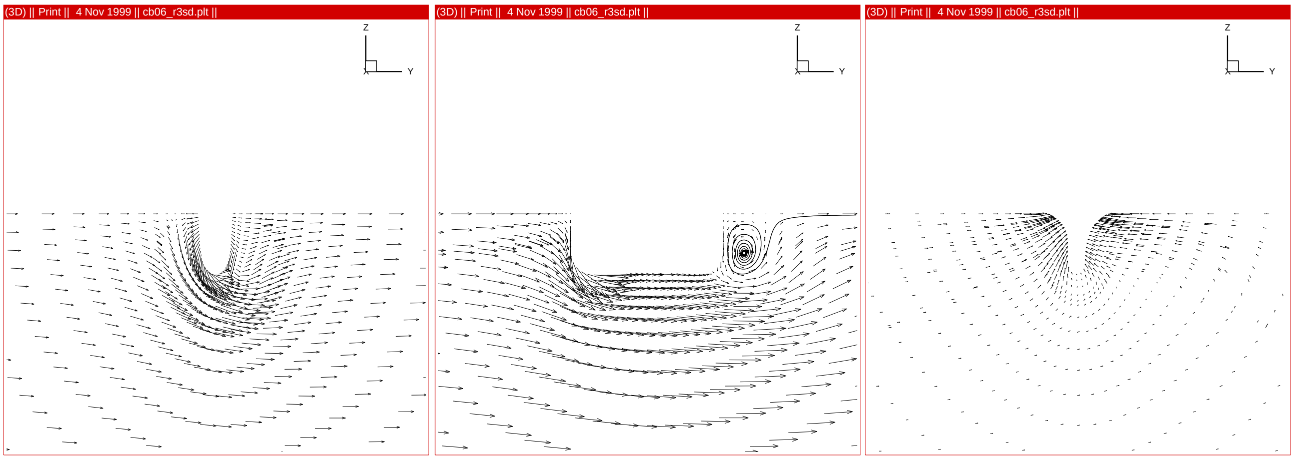

Figure 26: Cb=0.6, Steady Drift plus Turning: R/L=3, β=10

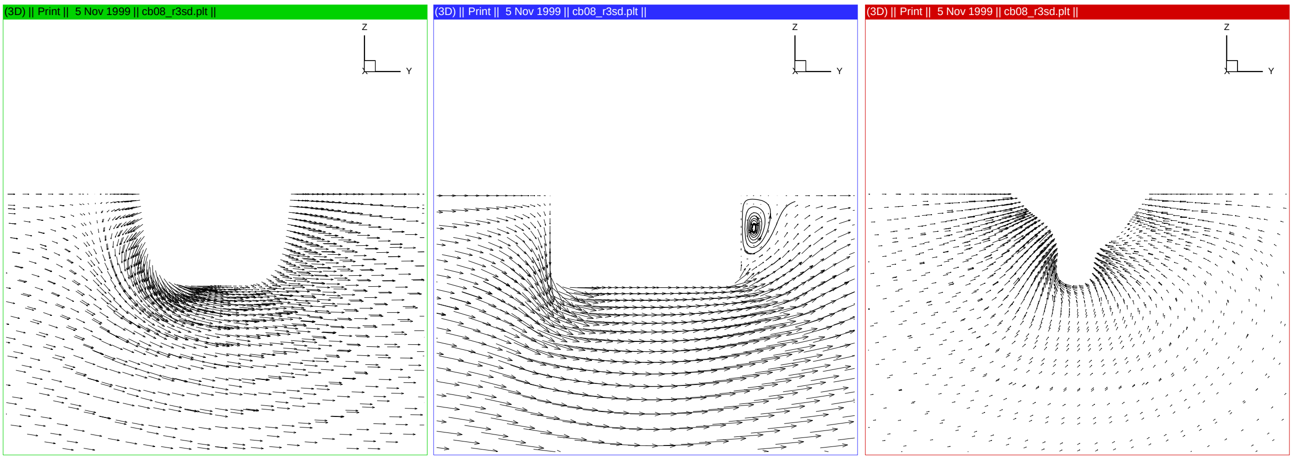

Figure 27: Cb=0.8, Steady Drift plus Turning: R/L=3, β=10

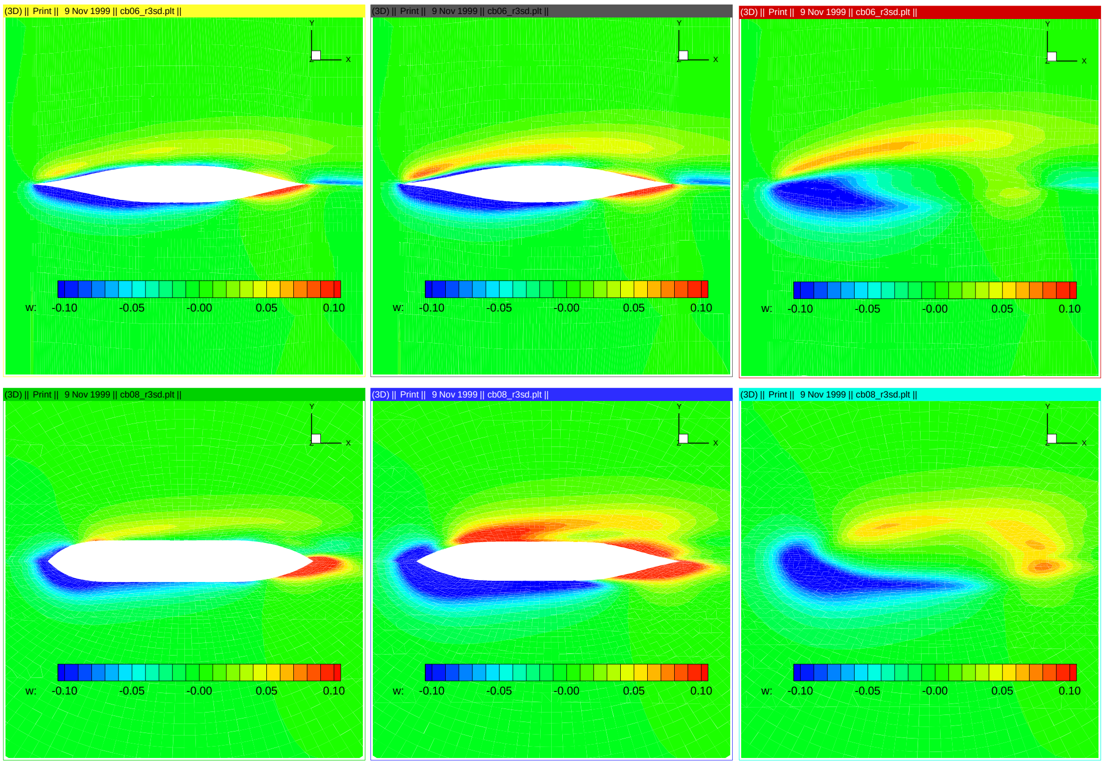

Figure 28: Cb=0.6 (top) and CB=0.8 (bottom): z-velocity contours plot; Steady Drift + Turning case R/L=3

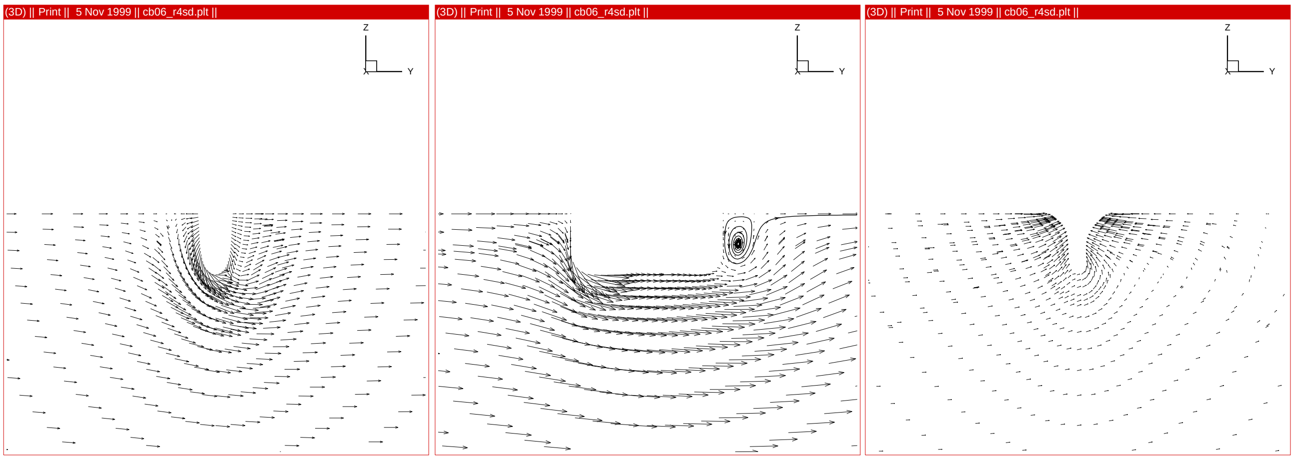

Figure 29: Cb=0.6, Steady Drift plus Turning: R/L=4, β=10

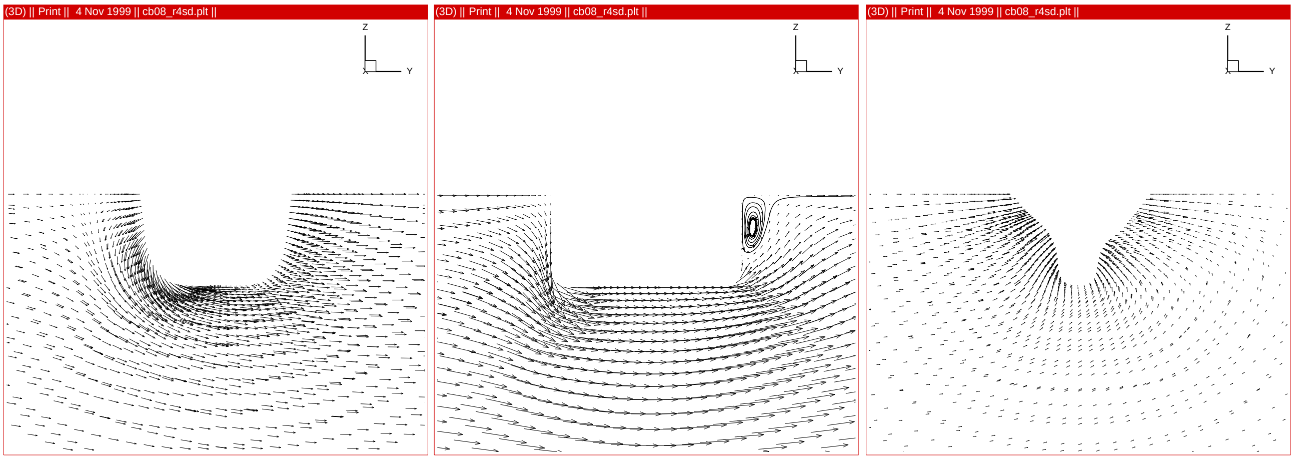

Figure 30: Cb=0.8, Steady Drift plus Turning: R/L=4, β=10